Available online at www.sciencedirect.com
SCIENCE DIRECT
Journal of Catalysis 233 (2005) 186–197
JOURNAL OF CATALYSIS
www.elsevier.com/locate/jcat

A novel efficient Au–Ag alloy catalyst system: preparation, activity, and characterization

Ai-Qin Wang [a], Jun-Hong Liu [a], S.D. Lin [b], Tien-Sung Lin [c], Chung-Yuan Mou [a,*]

[a] *Department of Chemistry and Center of Condensed Matter Science, National Taiwan University, Taipei, Taiwan*
[b] *Department of Chemical Engineering, Yuan Ze University, Chung-Li, Taoyuan 320, Taiwan*
[c] *Department of Chemistry, Washington University, St. Louis, MO 63130, USA*

Received 10 January 2005; revised 9 March 2005; accepted 24 April 2005

Available online 25 May 2005

Abstract

We present a novel efficient catalyst, Au–Ag alloy nanoparticles supported on mesoporous aluminosilicate. The catalysts were applied to the low-temperature CO oxidation reaction. The sample was prepared in one pot, in which the formation of nanoparticles was coupled in aqueous solution with the construction of mesoporous structure. Both XRD and TEM characterizations show that the alloy particles are much larger than the monometallic gold particles and become even bigger with an increase in the amount of Ag. We shall demonstrate that such large particles with an average particle size of about 20–30 nm exhibit exceptionally high activity for CO oxidation at low temperatures. Moreover, the activity varies with the Au/Ag molar ratios and attains the best conversion when Au/Ag is 3:1. The presence of excess H_2 deactivates the alloy activity completely at room temperature. UV–vis and EXAFS confirm the Au–Ag alloy formation. XPS results show that the alloy catalysts are in the metallic state, and they have a greater tendency to lose electrons than do the monometallic catalysts. EPR results show there is an O_2^- species on the catalyst surface, and the intensity of the O_2^- species becomes the strongest at Au/Ag = 3:1. The catalytic activity coincides with the magnitude of O_2^- EPR signal intensities. Based on the spectroscopic study and catalytic activity measurements, a reaction mechanism has been proposed.

Keywords: Gold; Silver; Nanoparticle; CO oxidation; Mesoporous aluminosilicate

1. Introduction

Supported gold catalysts have been extensively investigated for low-temperature CO oxidation since Haruta's pioneering work [1–5]. It has been found that the catalytic activity of gold is remarkably sensitive to the size of the gold particle [6–10], the preparation methods [11–14], and the nature of the support [15–19]. Therefore, most of the reported works focused on the tuning of the particle size, modification of the support, and the pretreatment conditions [20–22]. Both experimental works and theoretical calculations show that the adsorption and activation of O_2 are the key steps in this reaction [23–26]. For active supports, such as Fe_2O_3, and TiO_2, the oxygen activation occurred on the support surface and the CO oxidation reaction occurred at the periphery between the support and the gold nanoparticles [2,16]. Thus, the requirement for very small gold nanoparticles may arise mainly from larger contact peripherals. However, in the case of inert supports, such as SiO_2, the adsorption of both CO and O_2 has to be carried out on the gold surface. Then the size of the gold nanoparticle plays a paramount role in this reaction [27,28].

Conceivably, an alternative way to modify the gold-based catalysts is to search for a second metal that can form an alloy with gold and possesses stronger affinity with O_2 than gold. That is, where two different metal atoms are in intimate proximity to each other, as in an alloy, the activated O_2 can easily react with the activated CO at a neighboring gold atom to give the product CO_2. Some success along this line has

* Corresponding author. Fax: +886 2 2366 0954.
E-mail address: cymou@ntu.edu.tw (C.-Y. Mou).

0021-9517/$ – see front matter
doi:10.1016/j.jcat.2005.04.028

recently been reported. Häkkinen et al. [22] have confirmed that doping Au with Sr significantly changes the bonding and activation of O_2 compared with that in the pure gold, resulting in an enhanced activity for CO oxidation. However, their soft-landing method is not suitable for the practical preparation of a large amount of catalyst. Guczi et al. [29,30] investigated the Au–Pd bimetallic system for CO oxidation. They found that when supported on SiO_2, the activity of bimetallic catalyst was inferior to that of monometallic Pd/SiO_2 catalyst. When supported on TiO_2, the bimetallic catalyst exhibited a slightly synergistic effect. This may due to the fact that Pd adsorbs O_2 very strongly and weakens the role of gold. Baiker et al. [31] used amorphous metal alloy as the precursor for the preparation of $Au–Ag/ZrO_2$ and found that the alloy catalyst shows good activity and stability for CO oxidation. However, because Au/ZrO_2 itself is a very active catalyst, the alloying of gold with silver did not seem to have a significant promoting effect.

It is known that the electron transfer from metal to O_2 is a key factor for the chemisorption of oxygen on a metal surface [32,33]. Electron transfer is difficult on a Au(111) surface, since the gold surface has a high work function [34]. Relative to gold, both Cu and Ag have a larger electron-donating ability. It is known that the adsorption of O_2 occurs most easily on Cu, and next on Ag, but not on Au. On the other hand, both gold and copper are able to adsorb CO, but silver is not [34,35]. Thus, combining gold with silver may be an alternative avenue to achieving a catalyst with higher activity for CO oxidation.

In our earlier work, we developed a simple one-pot method to incorporate surfactant-protected gold particles into mesoporous MCM-41 [36]. Because the gold particles obtained with this method have a large size of about 7–8 nm, the catalytic activity is not so high. More recently, Au–Ag alloy nanoparticles supported on mesoporous aluminosilicate were prepared by this one-pot synthesis method, with the use of hexadecyltrimethylammonium bromide (CTAB) both as a stabilizing agent for nanoparticles and as a template for the formation of mesoporous structure [37]. The alloy catalyst exhibited exceptionally high activity in low-temperature (250 K) CO oxidation. Although monometallic Au@MCM-41 and Ag@MCM-41 show no activity at this temperature, the Au–Ag alloy system shows a strongly synergistic effect in high catalytic activity.

Our previous communication was a brief report on catalytic activities of the Au–Ag alloy nanocatalyst [37]. A fundamental understanding from detailed characterizations of the catalytic system was not available up to now. In this work, we prepared a series of Au–Ag alloy catalysts supported on MCM-41 to study the variations of catalytic activities with respect to changing temperature and composition. Many characterization techniques were used to study the catalyst system, such as nitrogen adsorption, XRD, XPS, EXAFS, UV–vis, and EPR spectroscopy. Based on these detailed studies, we then discuss the origin of the unique synergistic effect in the catalysis of CO oxidation.

2. Experimental

2.1. Preparation of catalysts

To synthesize the gold–silver alloy nanoparticles supported on mesoporous aluminosilicate (denoted AuAg@MCM) in one pot, the first step is to prepare the alloy Au–Ag nanoparticles in aqueous solution. A proper amount of $HAuCl_4$ (Aldrich) and $AgNO_3$ (Acros) was added into an aqueous solution of quaternary ammonium surfactant C_{16}TMAB (Acros) to form a clear yellow solution. Then, $NaBH_4$ solution was added dropwise, and a dark-red solution was formed. The Au–Ag alloy nanoparticle solution was then poured directly into a sodium aluminosilicate solution with a pH adjusted to about 9.0, and a red-colored precipitate formed immediately. The gel solution was then transferred to an autoclave to undergo hydrothermal reaction at 100 °C for 6 h. Overall, the molar ratio in the aluminosilicate gel was 1.0 SiO_2:0.042 $NaAlO_2$:0.18 C_{16}TMAB:493 H_2O, and the total metal loading was 8 wt%. Unless otherwise mentioned, the Au/Ag molar ratios discussed below are the nominal values as in the precursor solution, and they are consistent with the compositions measured by energy-dispersive X-ray microanalyses (EDX) (see Table 1). After filtration, washing, drying, and calcination at 560 °C in air, the AuAg@MCM was obtained. Before the following characterizations and activity measurements, the catalysts were reduced in 10% H_2/N_2 at 600 °C for 1 h.

2.2. Characterization

The UV–vis spectra were recorded on a Hitachi U-3010 UV–vis spectrophotometer at ambient temperature, operating in the reflection mode at a resolution of 2 nm, with barium sulfate as a standard for the background correction.

TEM images of AuAg@MCM were obtained with a JEOL JEM-2010 transmission electron microscope with an operating voltage of 200 kV. Samples were dispersed in ethanol, and a drop of the suspension was fixed on a microgrid covered with amorphous carbon film.

Powder X-ray diffraction (XRD) patterns were collected on a Philips PW 1830 instrument operating at a voltage of 45 kV and a current of 40 mA with Cu-K_α radiation in the 2θ range from 1.5° to 10° and from 20° to 80°.

Nitrogen adsorption–desorption isotherms were obtained at 77 K on a Micromeritics ASAP 2010 apparatus, and the pore size distribution was calculated from the nitrogen adsorption isotherm by the BJH (Barrett–Joyner–Halenda) method.

XPS spectra were obtained with a VG ESCALAB 250 equipped with a monochromated Al-K_α radiation source (1486.6 eV) under a residual pressure of 10^{-9} Torr. For charge compensation, a flood gun with variable electron voltage (from 6 to 8 eV) was used. The raw data were corrected for substrate charging with the binding energy of the Si_{2p} peak (103.3 eV) on an aluminosilicate support as a reference. The measured spectra were fit by a least-squares

procedure to a product of Gaussian–Lorentzian functions after subtraction of background noise. No traces of chlorine or bromine were detected by XPS on the reduced catalyst samples. The concentration of each element was calculated from the area of the corresponding peak, calibrated with the sensitivity factor of Wagner [38].

Electron paramagnetic resonance (EPR) spectra were recorded at 84 K with a Bruker EMX spectrometer working in the X-band (9.53 GHz). A weighted catalyst of 20 mg was placed inside a 4-mm O.D. quartz tube with greaseless stopcocks. Before each measurement, the reduced catalyst was first exposed to air and then evacuated at room temperature until the residual pressure was below 1×10^{-3} Torr.

The X-ray absorption fine structure (XAFS) spectra were recorded at the Beam Line 17C and 01C at the National Synchrotron Radiation Research Center (NSRRC), Hsinchu, Taiwan. The electron storage ring was operated at 1.5 GeV with a beam current of 100–200 mA. Both the Au L_{III}-edge and Ag K-edge absorbance of powder catalysts were measured in transmission geometry. The XAFS data analysis was carried out with the UWXAFS package.

2.3. Activity measurements

The CO oxidation reaction was performed in a continuous-flow fixed-bed microreactor. A total of 0.04 g of catalyst was used in each experiment. Before measurement, the catalyst was pre-reduced in situ in 10% H_2 in N_2 at 600 °C for 1 h. The reactant gases were purified by 4-Å molecular sieves, then mixed and passed into the reactor. Thus, the water vapor content in the reactant stream was no more than 4 ppm. The reactant flow consisted of a mixture of 1% CO and 4% O_2, with He as the balance. A total gas flow of 66.7 ml/min was applied, corresponding to a GHSV of about 100,000 ml/(g_{cat} h). The reactants and products were analyzed on line with a HP6890 gas chromatograph equipped with a Carboxen1000 column and a TCD detector. The CO conversion is defined as the amount of CO_2 produced divided by the total amount of CO fed to the catalyst. The selectivity for CO oxidation in the presence of excess H_2 is defined as

$$S = \frac{0.5[CO_2]}{[O_2]_{in} - [O_2]_{out}} \times 100\%,$$

where $[O_2]_{in}$ is the inlet O_2 concentration, $[O_2]_{out}$ is the outlet O_2 concentration, and $[CO_2]$ is the CO_2 production concentration.

3. Results

3.1. Physical properties of catalysts

Table 1 lists the BET surface area, pore volume, and average pore size of the catalysts with different Au/Ag molar ratios. The BET surface areas of the catalysts were between 800 and 900 m^2/g, and the pore size was between 2.3 and 2.4 nm. The pore volume was relatively large compared with traditional MCM-41 material. This arose from the fast neutralization procedure used in this work, which led to the formation of relatively nanosized particles of the support material, ranging from 50 to 100 nm, thus producing a large amount of interparticle textural porosity [39,40]. It is clear that the textural properties of these catalysts at various Au/Ag compositions are quite similar.

Table 1
Chemical composition and textural properties of catalysts and estimated metal particle size

Au/Ag (molar ratio)		Pore size (nm)	Pore volume[a] (cm^3/g)	BET surface area (cm^2/g)	Metal particle size (nm)	
Nominal	EDX				XRD	TEM
1/0	1/0	2.38	1.61	836	6.7	6.7
8/1	na[b]	2.36	1.71	843	19.1	21.5
5/1	5.37	2.39	1.85	812	17.1	21.4
3/1	3.07	2.35	1.70	844	17.5	24.1
1/1	1.56	2.38	1.96	862	24.9	52.3
0/1	0/1	2.33	2.00	901	23.2	21.0

[a] Total pore volume obtained from $P/P_0 = 0.99$.
[b] Not analyzed.

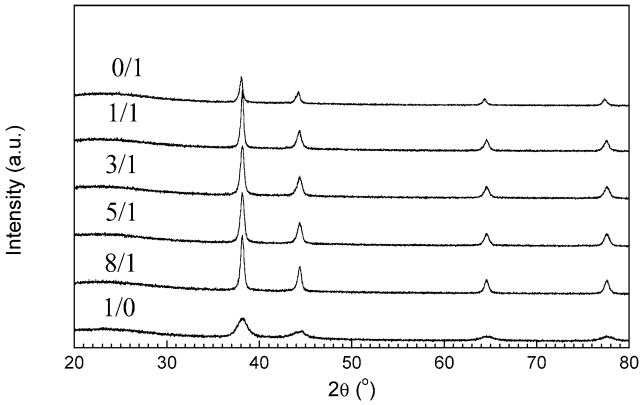

Fig. 1. Wide-angle XRD patterns of Au–Ag@MCM with different Au/Ag molar ratios after calcinations and then reduction.

Fig. 1 shows wide-angle XRD patterns of catalysts with different Au/Ag ratios after they were calcined at 560 °C and then reduced by H_2 at 600 °C. We observed that pure Ag@MCM and all of the bimetallic Au–Ag catalysts have the same XRD patterns as Au@MCM, which is characterized by four peaks positioned at $2\theta = 38.2°$, 44.3°, 64.5°, and 77.6° due to the (111), (200), (220), and (311) lattice planes [41]. Since silver has the same structure (fcc) and lattice constant as gold (0.409 nm versus 0.408 nm), they have the same XRD patterns, and one cannot distinguish gold–silver alloy from either monometallic phase from the XRD patterns. It is worth noting that all of the bimetallic samples, as well as Ag@MCM, have sharper XRD peaks than the Au@MCM. This indicates that the metal particle size in the bimetallic samples is larger than that in Au@MCM. From Scherrer's equation, the average metal particle size in Au@MCM is estimated to be 6.7 nm, and the Au–Ag bimetallic particle size is about 20 nm (see Table 1).

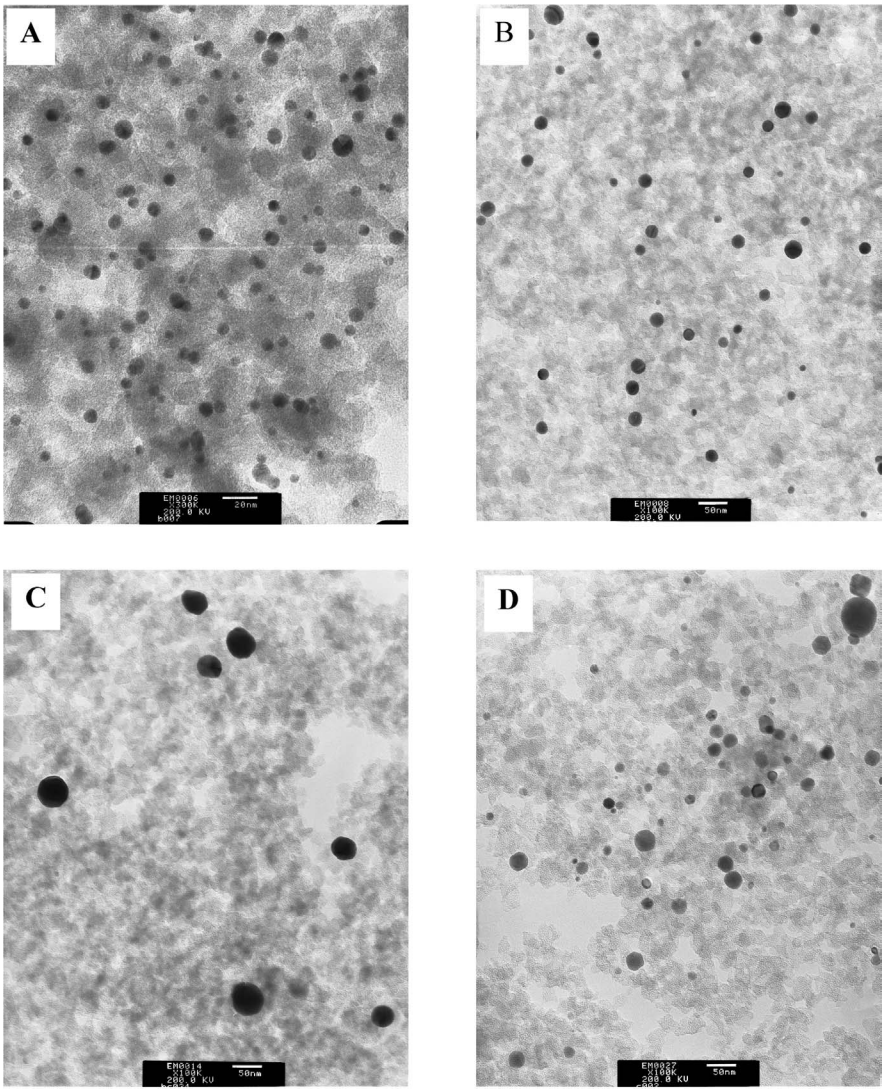

Fig. 2. TEM images of Au–Ag@MCM for the following Au/Ag molar ratios: (A) 1/0; (B) 5/1; (C) 1/1; (D) 0/1. The scale bar is 50 nm except in A (20 nm).

3.2. TEM characterization

For CO oxidation catalyzed by pure gold nanoparticles, the size of the gold nanoparticle is the most important factor. To determine the metal particle size and size distribution of Au–Ag bimetallic catalysts, a high-resolution TEM technique was employed. The images are shown in Fig. 2, and the particle size histograms are presented in Fig. 3. Consistent with the XRD results, the gold particle size of pure Au@MCM is small, about 6.7 nm. However, in the case of Au–Ag bimetallic catalysts, the particle size became much larger. Samples with Au/Ag ratios of 5:1, 3:1, and 1:1 had average particle sizes of about 21.4, 24.1, and 52.3 nm, respectively. The particle size determined by TEM is somewhat larger than that estimated by XRD (see Table 1), especially for the Au–Ag alloy catalysts, because accurate estimation by XRD line-width becomes instrument-limited when the particle size becomes large and the XRD peaks become very sharp. It must be pointed out that even with a high-resolution TEM operated at 200 kV with a magnification of 600,000, we did not observe very small nanoparticles with a size below 5 nm in the alloy catalysts.

3.3. UV–vis absorption spectra

Both Au and Ag, as well as Au–Ag alloy, show characteristic UV–vis absorption peaks due to their surface plasma resonance band [42–45]. Fig. 4A shows UV–vis spectra for catalysts with different Au/Ag ratios. For the pure Au@MCM and pure Ag@MCM, respectively, absorption bands with maxima at 525 and 394 nm were observed, which is consistent with the reported spectra [42,43]. All Au–Ag bimetallic catalysts show absorption peaks located between the absorption bands of pure Au and pure Ag, and the absorption peaks shift to red with an increase in Au/Ag

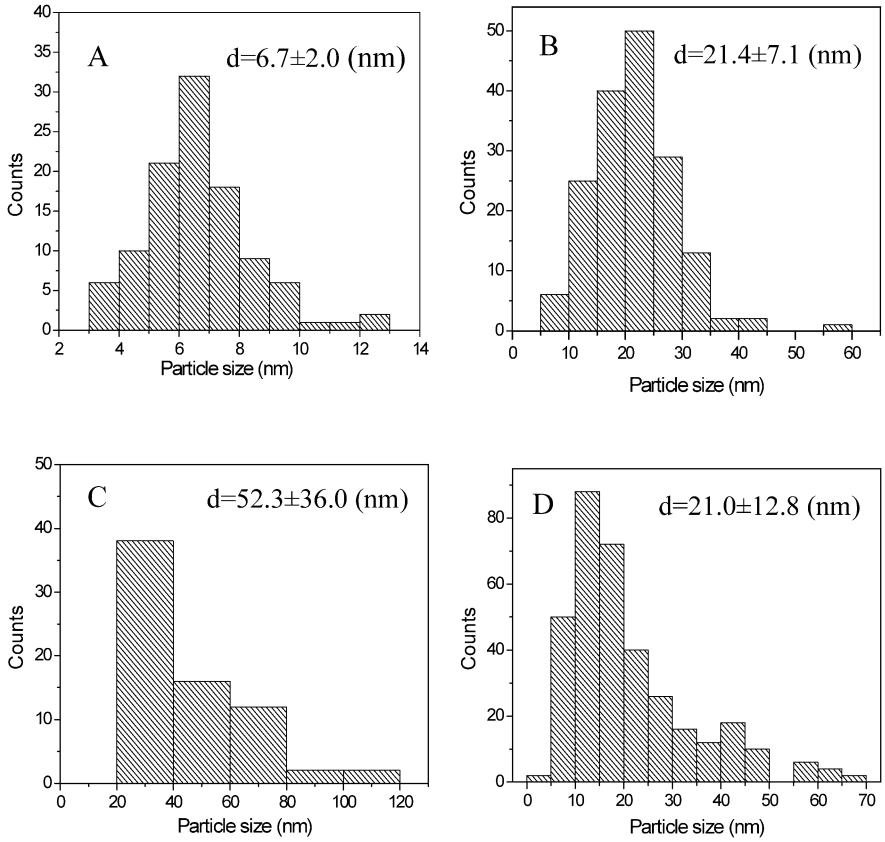

Fig. 3. Size histogram of Au–Ag@MCM with Au/Ag molar ratio of (A) 1/0; (B) 5/1; (C) 1/1; (D) 0/1.

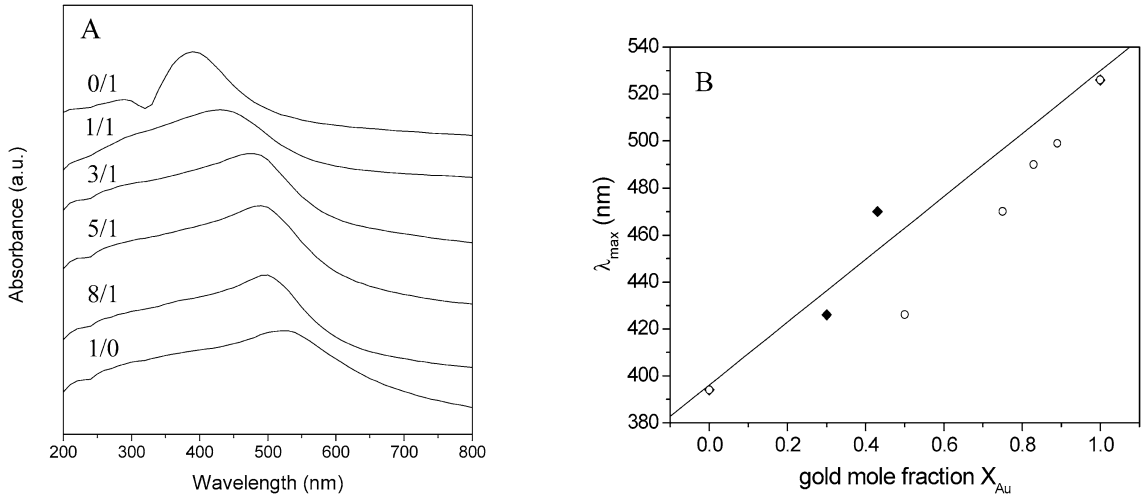

Fig. 4. (A) UV–vis absorption spectra of Au–Ag@MCM with different Au/Ag molar ratios; (B) absorption maximum of surface plasma band plotted against (◯) the nominal molar fraction of Au in Au–Ag@MCM and (♦) surface molar fraction of Au determined by XPS.

molar ratios. For all of the investigated Au–Ag bimetallic catalysts, only one absorption peak was observed, which is an indication of Au–Ag alloy formation. When we tried to correlate the maximum absorption wavelength λ_{max} with the nominal gold mole fraction of these Au–Ag bimetallic catalysts, the function deviated from a linear relationship (Fig. 4B). This suggests that after calcination and reduction at high temperatures, the surface chemical composition of the Au–Ag bimetallic catalysts is different from that of the bulk. This has been confirmed by XPS measurements of the surface composition. When we use the gold mole fraction determined by XPS instead of nominal values, we obtained a linear relationship (dark points in Fig. 4B). Since XPS is a surface-sensitive technique, the surface composition would have been a better predictor for the λ_{max} of the surface plasmon resonance (SPR) band.

3.4. XPS spectra

To determine the oxidation state and the charge transfer tendency between gold and silver in the alloy catalysts, we conducted an X-ray photoelectron spectroscopy (XPS) characterization of the catalysts with various Au/Ag ratios after reduction with H_2; the results are given in Fig. 5 and Table 2. For the pure Au@MCM catalyst, the binding energy of $Au_{4f_{7/2}}$ is 83.4 eV, which is lower than that of bulk metallic gold (84.0 eV). Such a negative shift has also been observed with gold catalyst by other groups [17,46,47]. Radnik et al. [46] studied the binding energy shifts of SiO_2-supported gold nanoparticles. They found that hydrogen pretreatment lowered the binding energy of $Au_{4f_{7/2}}$ to 83.3 eV, which is in agreement with our results. The authors proposed that the hydrogen pretreatment may alter the shape of gold particles, which is responsible for the binding energy shift. In their catalyst system, gold is in the metallic state. Similarly, Arrii et al. [17] observed the dependence of the $Au_{4f_{7/2}}$ binding energies on different kinds of support. On TiO_2 and Al_2O_3 supports, $Au_{4f_{7/2}}$ binding energy had a negative shift of −0.6 and −0.9 eV, respectively. Although a large shift (up to −1.1 eV for the used Au/TiO_2) was observed, the authors concluded that the gold is in the metallic state, because they did not observe any peaks of oxidized gold species (located around 85.5 and 86.3 eV). They attributed such a negative shift to the possible electron transfer from the support to the particle. Hence, based on the above reports [17,46], we propose that Au in Au@MCM is of a metallic nature, and the 0.6 eV difference in $Au_{4f_{7/2}}$ we observed between Au@MCM and bulk metallic gold is due either to the interaction between support and Au nanoparticle or to the hydrogen pretreatment we used. On the other hand, the binding energy of $Ag_{3d_{5/2}}$ in the pure Ag@MCM was 368.5 eV, which is slightly higher than that of bulk metallic Ag (368.3 eV). Moreover, for the bimetallic catalyst samples, Au_{4f} binding energies shifted to higher values compared with monometallic Au@MCM, and closer to that of the bulk metallic Au. This suggested that in all of the gold-containing samples, the gold existed in the metallic state, and alloying of Ag with Au seems to give gold a slightly greater tendency to lose electrons. On the other hand, compared with the monometallic Ag@MCM, alloying of Au with Ag makes the Ag_{3d} binding energy shift to lower values. The $Ag_{3d_{5/2}}$ binding energy shifted to 368.0 eV for a Au/Ag ratio of 3:1, from the 368.5 eV of pure Ag@MCM. This implies that through alloying with gold, the silver has a greater tendency to lose electrons. In summary, the observation that binding energy changed with the Au/Ag ratios suggested that alloying Au with Ag gives both metals a greater tendency to lose electrons.

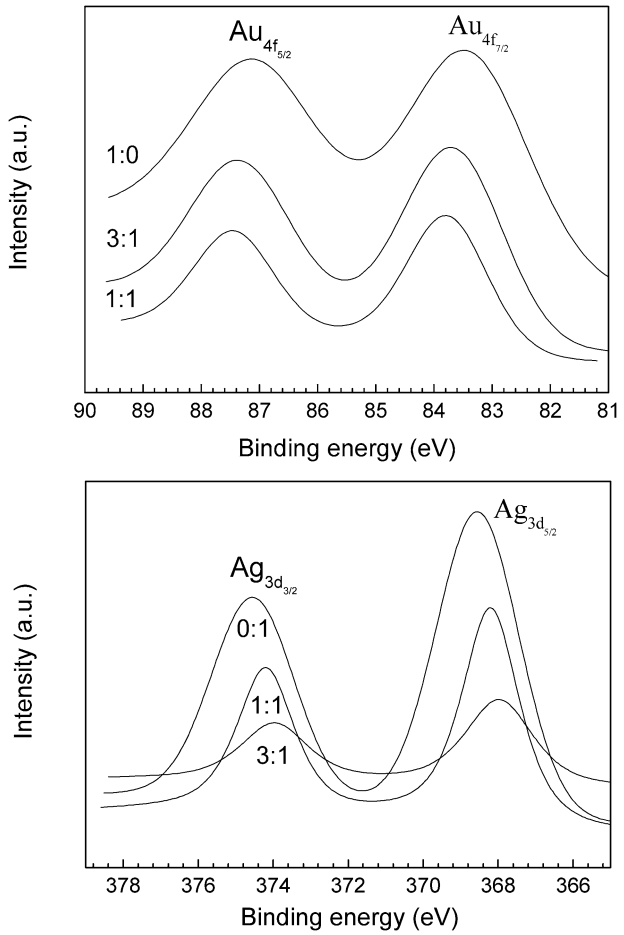

Fig. 5. XPS spectra of Au–Ag@MCM with different Au/Ag molar ratios.

Table 2
Binding energies and surface compositions of catalysts determined by XPS

Molar ratio	$Au_{4f_{7/2}}$ (eV)	$Au_{4f_{5/2}}$ (eV)	$Ag_{3d_{5/2}}$ (eV)	$Ag_{3d_{3/2}}$ (eV)	Au/Si (mole)	Ag/Si (mole)	Au/Ag (mole)
Au/Ag = 1/0	83.4	87.2	–	–	0.0274	–	1/0
Au/Ag = 1/1	83.8	87.5	368.2	374.2	0.0111	0.0255	0.43
Au/Ag = 3/1	83.6	87.3	368.0	374.0	0.0165	0.0221	0.75
Au/Ag = 0/1	–	–	368.5	374.5	–	0.0500	0/1

On the other hand, we note from Table 2 that the surface composition of the catalysts is quite different from the total compositions. For example, the catalyst with a total Au/Ag molar ratio of 3:1 has a surface Au/Ag molar ratio of 0.75:1, indicating that the catalyst surface is enriched with Ag. The same trend has been observed by another group [41].

3.5. EXAFS results

In order to confirm the Au–Ag alloy formation on the mesoporous support, we used the EXAFS technique to determine the atom type and number of atoms nearest to Au and Ag; results are listed in Tables 3 and 4. The coordination number (CN) of Au–Au and Au–Ag reflects the particle size and the degree of alloy formation [48]. From the Au L_{III}-edge in Table 3, we note that the bond distance for Au–Au and Au–Ag is almost the same, about 2.86 Å. The coordination number of gold is near that of bulk Au, 12, and is independent of the Au/Ag ratios. On the other hand, the ratios of CN for Au–Au and Au–Ag are very close to the

Table 3
Au L_{III}-edge XAFS analysis of the AuAg@MCM catalysts after reduction

Au/Ag (molar)	Shell	R (Å)	CN	σ^2
1/0	Au–Au	2.858 ± 0.002	10.9 ± 0.5	0.009 ± 0.0002
5/1	Au–Au	2.860 ± 0.008	9.1 ± 1.3	0.008 ± 0.0007
	Au–Ag	2.858 ± 0.024	1.7 ± 1.0	0.008 ± 0.004
3/1	Au–Au	2.851 ± 0.008	8.0 ± 1.2	0.010 ± 0.0009
	Au–Ag	2.865 ± 0.018	2.9 ± 1.0	0.011 ± 0.003
1/1	Au–Au	2.860	5.6 ± 0.6	0.008 ± 0.0006
	Au–Ag	2.862 ± 0.002	4.6 ± 0.5	0.008 ± 0.0006

Table 4
Ag K-edge XAFS analysis of the AuAg@MCM catalysts after reduction

Au/Ag (molar)	Shell	R (Å)	CN	σ^2
0/1	Ag–Ag	2.863 ± 0.003	8.8 ± 0.6	0.010 ± 0.0004
5/1	Ag–Ag	2.842 ± 0.015	2.1 ± 5.2	0.020 ± 0.035
	Ag–Au	2.849 ± 0.007	6.8 ± 2.5	0.008 ± 0.001
3/1	Ag–Ag	2.845 ± 0.020	1.6 ± 0.7	0.009 ± 0.003
	Ag–Au	2.849 ± 0.007	7.8 ± 1.0	0.009 ± 0.0007
1/1	Ag–Ag	2.858 ± 0.009	4.6 ± 0.7	0.009 ± 0.001
	Ag–Au	2.852 ± 0.009	3.6 ± 0.9	0.008 ± 0.001

nominal Au/Ag ratios. It should be pointed out that in the EXAFS data analysis, Au–O and Ag–O were also expected to fit the experimental data, but no results displaying a good fit were obtained. Therefore, our EXAFS results provide evidence for the Au–Ag alloy formation. Furthermore, they confirm that both Au and Ag are in the metallic state, and the Au–Ag alloy particles are large. This result is in agreement with the XPS and TEM results. From the Ag K-edge analysis presented in Table 4, we obtain the same conclusion as from the Au L_{III}-edge, but the quality of the data was not so good, because of the low concentration of Ag in the alloy samples.

3.6. EPR results

EPR is a highly sensitive technique for the study of redox processes, especially when they involve electron transfer species. In this work, EPR spectra were measured on catalysts with different Au/Ag ratios, so as to detect the presence of O_2^- and the effect of Au/Ag ratio on the intensities of O_2^-. The EPR results are illustrated in Fig. 6. Clearly, for all of the samples studied, we observed only one EPR signal at $g = 2.009 \pm 0.001$. Moreover, the signal intensity varies with the different Au/Ag ratios. Okumura studied the CO and O_2 interaction on Au/TiO_2 by the EPR technique [49]. In their system, they also observed the signal at $g = 2.009$, and they attributed it to the O_2^- radicals bonded to Ti^{4+} ions. Similarly, we can assign the signals at $g = 2.009 \pm 0.001$

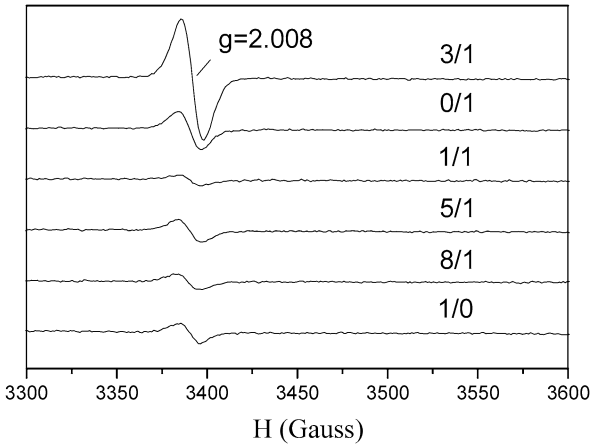

Fig. 6. EPR spectra of Au–Ag@MCM samples at 84 K. The samples were reduced with H_2, and then exposed to air. Prior to EPR measurements, the samples were out-gassed overnight at room temperature.

to O_2^- radicals bonded to metal ion. Since we also observed a very weak EPR signal of the O_2^- radicals on the aluminosilicate support without Au–Ag particles on it, the generation of O_2^- on the Au–Ag@MCM could be due either to electron transfer from the support to adsorbed O_2 on defect sites associated with tetrahedral Al on the mesoporous support, or to the electron transfer from alloy particles to the adsorbed O_2. However, in the present work, all catalysts have the same support, so the variation in EPR signal intensity should mainly come from the different ratios of Au/Ag. The intensities of O_2^- signals are in the following order: 3:1 (Au/Ag) > 5:1 > 8:1 > 1:1.

3.7. Catalytic behavior in CO oxidation

Fig. 7 shows the CO conversion at room temperature versus time on stream for pure metals (Fig. 7A) and alloys (Fig. 7C) supported on MCM-41. At room temperature, Au@MCM had a very low activity, whereas Ag@MCM did not exhibit any catalytic activity. In contrast, Au–Ag alloy catalysts show much higher (and more stable) activity than the corresponding monometallic catalysts at low temperatures. Moreover, the activity of alloy catalysts changed dramatically with the variation in Au/Ag ratios. The catalyst with a Au/Ag ratio of 3:1 has the highest activity on which CO is completely converted at room temperature. When the Au/Ag ratio was increased from 3:1 to 5:1 and 8:1, or decreased from 3:1 to 1:1, the activity decreased. On the other hand, it can be observed that the activity profiles versus reaction temperature observed over alloy catalysts (Fig. 7D) are quite different from that observed over monometallic catalysts (Fig. 7B). On pure metallic catalysts, both Au@MCM and Ag@MCM catalyst, the activity increased monotonically with increasing reaction temperature, which agrees with previous reports [3,4]. The activity of Au nanoparticles is higher than that of Ag. However, for Au–Ag alloy catalysts, the activity increased first with increasing temperature in the low temperature range (up to 80 °C), then

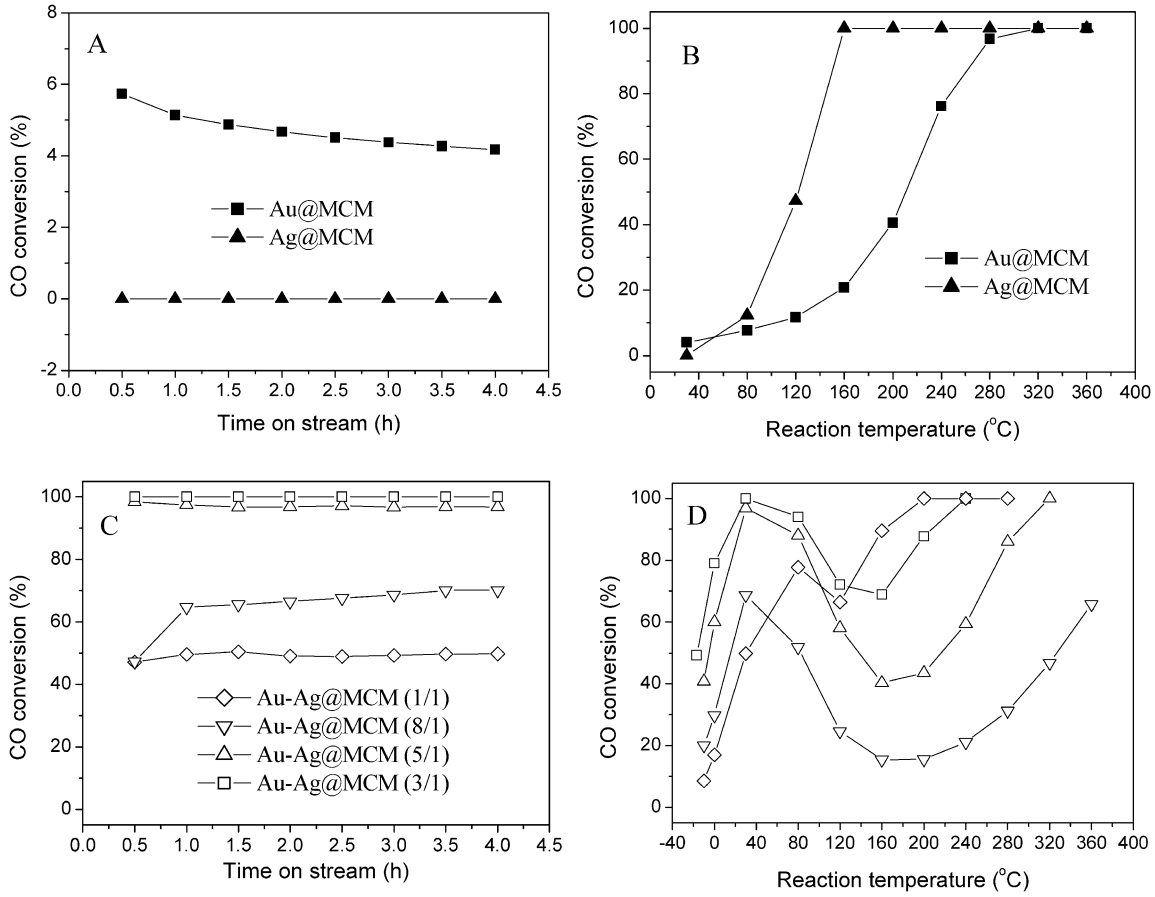

Fig. 7. (A) CO conversion at room temperature versus time-on-stream for pure metals supported on MCM-41; (B) CO conversion profile with reaction temperature for pure metals supported on MCM-41; (C) CO conversion at room temperature versus time-on-stream for alloy@MCM with different Au/Ag molar ratios. (D) CO conversion profile with reaction temperature for alloy@MCM. The reaction gas composition is: 1% CO, 4% O_2 and He as balance.

decreased with increasing temperature in the range of 80–160 °C. When the reaction temperature further increased from 160 to 300 °C, the activity increased again, as in the monometallic catalyst. Such an activity dip with the reaction temperature range between 80–300 °C suggests that there is a difference in reaction mechanism between monometallic and bimetallic catalysts.

When a large amount of H_2 is present in the reaction stream, the catalytic behavior of Au–Ag alloy is also quite different from that of Au catalyst. As shown in Fig. 8A, when the feed gas was switched to include an excess of H_2, CO conversion was increased from 4 to 9% at 30 °C over Au@MCM catalyst. With the reaction temperature increased to 80 °C, the CO conversion further increased to about 33%. However, when the H_2 gas was switched off, the CO conversion dropped from 34 to 6% at 80 °C. With the reaction temperature further increased to 120 °C, the CO conversion increased slightly. When H_2 was present again in the feed gas at 120 °C, the CO conversion went up again. Such an on-off cycle clearly demonstrates that the presence of excess H_2 in the feed gas greatly improved the activity of Au@MCM, whereas in contrast H_2 poisoned the CO oxidation reaction over the alloy catalyst Au–Ag@MCM. Even after H_2 was removed from the feed gas afterward, the activity was not restored (see Fig. 8B). Table 5 lists the CO conversion and O_2 selectivities observed over the Au@MCM and the Au–Ag@MCM catalysts. On the gold catalyst, the selectivity decreased from 100 to 21% when the reaction temperature was increased from room temperature to 80 °C. However, on the alloy catalyst, the selectivity remained at 100% when the reaction temperature rose from 80 to 120 °C. Such a completely different behavior implies that the alloy catalyst has an active site that is different from that of monometallic gold catalyst.

Table 5
Catalytic performances of Au@MCM and Au–Ag@MCM in the presence of excess H_2[a]

Temp. (°C)	Au@MCM		Au–Ag@MCM (Au/Ag = 3/1)	
	CO conv. (%)	O_2 selec. (%)	CO conv. (%)	O_2 selec. (%)
30	8.5	100	0	–
80	34.7	21.0	9.7	100
120	33.7	5.3	17.8	100
160	–	–	17.8	12.5
200	–	–	9.6	1.7

[a] The reaction conditions are: 1% CO, 4% O_2, 60% H_2, He as balance. Space velocity is 100,000 ml/(g_{cat} h).

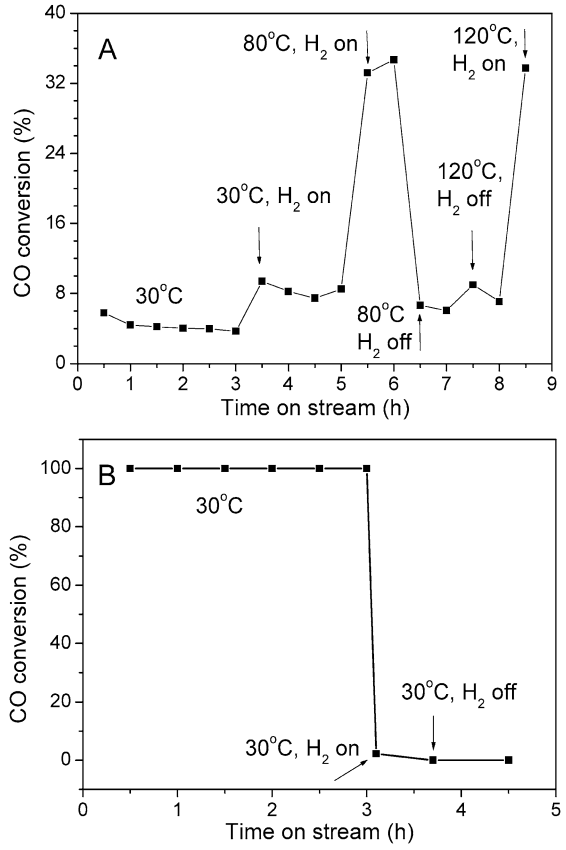

Fig. 8. Catalytic profiles of (A) Au@MCM and (B) Au–Ag@MCM (Au/Ag = 3/1) in the presence of rich hydrogen. The reaction gas composition: 1% CO, 4% O_2, 60% H_2 and He balance. The space velocity is 100,000 ml/(g_{cat} h).

The alloy catalyst not only has very high activity for CO oxidation at low temperatures, but also exhibits excellent stability. In fact, we observed that the CO conversion decreased from 100% only to about 95% after a 100-h run on the reaction stream.

4. Discussion

4.1. Formation of Au–Ag alloy nanoparticles on the mesoporous support

The direct preparation of Au–Ag alloy on mesoporous support by traditional deposition methods with the use of two precursors, such as $AgNO_3$ and $HAuCl_4$, is difficult [41,45]. However, recent developments in the preparation of gold–silver colloids in aqueous solution [44,45] provide an efficient approach to preparing the supported Au–Ag alloy nanoparticles. In the present work, we combine the formation of Au–Ag alloy nanoparticles with the construction of mesoporous structure in one pot. In this process, the surfactant CTAB played a dual role in stabilizing the nanoparticles and in templating the formation of mesoporous structure. The alloy nanoparticles were confirmed by XRD, TEM, UV–vis, and EXAFS, and the mesostructure was identified by low-angle XRD (not shown here) and N_2 adsorption–desorption. As shown in Table 1, the BET surface area of the catalyst was 800–900 m^2/g, only slightly less than that of the unloaded support, indicating that the metallic nanoparticles do not substantially block the pores. In fact, the average diameter of the channels of the support is about 2.4 nm (see Table 1), whereas either gold or gold–silver alloy particles are a bit bigger than the channel size. Therefore, the metal particles are too large to be imbedded inside the mesoporous channels. It is more likely that they are supported on the surface of the mesoporous aluminosilicate. The pore volumes of the catalysts are 1.6–1.9 cm^3/g, much larger than the usual pore volume (∼1.0 cm^3/g) of MCM-41. This is due to the large interparticle macropores formed between the nanosized support materials. Thus, the dual mesopores and macropores would facilitate the transport of reactants. On the other hand, the textural properties of the investigated catalysts are quite similar, so that the difference in catalytic activity among the catalysts could be assigned to the variation in the Au/Ag ratio.

4.2. Comparison of Au@MCM, Ag@MCM, and Au–Ag@MCM

In the present work, monometallic gold and silver and bimetallic gold–silver alloy catalysts were comparatively studied for their size and catalytic properties. When gold was deposited on the mesoporous aluminosilicate support by our one-pot method, the gold nanoparticles were well dispersed and had an average particle size of about 6.7 nm, as confirmed by XRD and TEM. In principle, such relatively large particles and the inert nature of the aluminosilicate support would lead to very low activity in CO oxidation over Au@MCM. Okumura et al. [27,28] have prepared Au nanoparticles on inert supports such as amorphous SiO_2 and SiO_2–Al_2O_3, as well as ordered mesoporous support MCM-41, by CVD and the impregnation method, respectively. They found that on such inert supports, only for gold nanoparticles with a size below 4 nm, as prepared by the CVD method [27], could high catalytic activity be obtained. Our catalytic results on Au@MCM are in agreement with the literature reported. Schubert et al. [16] attributed such a critical size effect of gold on inert supports to the reaction mechanism in which the activation of both oxygen and carbon monoxide was conducted on gold nanoparticles.

On the other hand, for the pure Ag@MCM, although it is completely inactive at room temperature, it attains higher activity than Au@MCM as the temperature is increased: 50% CO conversion at 120 °C and 100% conversion at 160 °C. This is in contrast to Au@MCM, which reaches 100% CO conversion only at about 320 °C. However, from XRD in Fig. 1 and the estimated particle size in Table 1, we note that Ag@MCM has a much larger particle size than Au@MCM (21.0 nm versus 6.7 nm). This suggests that the catalytic mechanism on Au@MCM and Ag@MCM may be differ-

ent. Qu et al. [50] recently reported that Ag/SiO_2 with large silver particles (>20 nm) shows activity in the CO oxidation reaction. This may arise from the easy adsorption and activation of oxygen on silver surfaces.

In contrast, the catalytic behaviors of gold–silver alloy catalysts are different from those of either of the monometallic catalysts. Strong synergistic effects were found with the promotion of the catalytic activities. All of the Au–Ag alloy catalysts in this work gave much higher activity than the monometallic catalysts. Previously, Venezia et al. [29, 51] investigated the Au–Pd and Ag–Pd bimetallic catalysts for CO oxidation. However, both Au–Pd and Ag–Pd alloy catalysts were less active than the pure Pd catalyst, showing no synergistic effect. Our work presents the first success in the synergistic effect of gold alloy nanoparticles for CO oxidation.

An important feature of such gold–silver alloy catalysts is that the catalytic activity can be tuned by variation of the Au/Ag molar ratios. When the Au/Ag ratio decreased from 8:1 to 5:1 and to 3:1, the CO conversion at room temperature increased from 70 to 97 and 100%. However, with a further decrease in the Au/Ag ratio to 1:1, the CO conversion dropped to about 50% (the values obtained after a 4-h run). A careful examination of the particle size of these alloy catalysts revealed that the particle size cannot account for the activity change with the Au/Ag ratio. The catalysts with Au/Ag ratios of 3:1, 5:1, and 8:1 have comparable particle sizes (see Table 1 and Figs. 2 and 3), whereas their activities follow the order of 3:1 > 5:1 > 8:1. On the other hand, for these three samples, the activity order agrees well with the intensity order of O_2^- as determined by EPR measurements. This seems to suggest that the generation of O_2^- is important in CO oxidation. Interestingly, the activation of O_2 to O_2^- species is dependent on the Au/Ag composition.

The electronic properties of gold are modified through alloying with Ag, as observed in the binding energy shift in XPS spectra. As described in Section 3.4, compared with monometallic Au@MCM and Ag@MCM, the Au_{4f} binding energy in Au–Ag alloy catalysts underwent a positive shift, whereas the Ag_{3d} binding energy in alloy catalysts underwent a negative shift. In consideration of the slight degree of the binding energy shift, to exclude the experiment error, the XPS experiment has been repeated three times, and the same shift trend has been obtained. Therefore, we believe that there has been a charge transfer. Generally, a higher oxidation state leads to a higher binding energy. This is the case for Au [52]. Hence, the positive shift of Au_{4f} implied that Au in alloy catalysts has a greater tendency to lose electrons than Au in Au@MCM. On the other hand, the opposite is true for Ag, and a higher oxidation state leads to a lower binding energy value for Ag species. For example, the binding energy of $Ag_{3d_{5/2}}$ in the metallic state is 368.3 eV, whereas it is 367.6 eV in the oxidic state (Ag_2O). Thus, the negative shift of Ag_{3d} implies that Ag in alloy catalysts can lose electrons more easily than Ag in Ag@MCM. Especially for the sample with a Au/Ag ration of 3:1, the binding energy of $Ag_{3d_{5/2}}$ shifted from 368.5 to 368.0 eV, which is between metallic Ag (368.3 eV) and oxidic Ag^+ (367.6 eV). This seems to suggest that there is some sort of oxidic Ag species on the Au–Ag alloy catalyst surface. Considering that the reduced catalyst samples were exposed to the air before XPS analysis, we think that O_2 was adsorbed to the catalyst surface during this process and there was partial electron transfer from Ag to adsorbed O_2, resulting in the formation of O_2^-. According to the literature [22], in CO oxidation, an electron transfer from metal to the antibonding orbital of the O_2 molecule would weaken O–O bonding, thus improving the oxygen activation. Therefore, from our XPS and EPR results, we conclude that the adsorption and activation of oxygen on the catalyst surface are improved by the alloying of Au with Ag in suitable molar ratios.

Furthermore, when the nominal Au/Ag ratio is 3:1 or 5:1, the corresponding surface Au/Ag ratios are 0.75:1 and 0.43:1, respectively, indicating the enrichment of Ag on the surface. Previously, Iizuka et al. also observed an enrichment of Ag impurity on gold nanoparticles [53]. Such a surface composition may favor the synergistic interaction between Au and Ag and enhance the catalytic activity.

The second important feature of the Au–Ag alloy catalyst as compared with monometallic catalysts is the unusual variation of the CO conversion curve with respect to the reaction temperature. As is well known for supported monometallic Au or Ag catalysts, CO conversion usually increases monotonically with the temperature. However, for the Au–Ag alloy catalysts, CO conversion decreased dramatically in the temperature range of 80–160 °C with increasing temperature. We believe this feature may be related to the differences between the mechanism of the Au–Ag alloy catalyst and the monometallic one [37]. In a recent report by Daté et al. [54], a similar phenomenon was observed on Au/SiO_2 when a certain concentration of moisture was present in the feed stream. The authors attributed such an activity dip to the desorption of moisture at higher temperatures, since the moisture was thought to be a prerequisite for the activity of Au/SiO_2 at lower temperatures, in which it assisted the adsorption and activation of oxygen. Similar to the role of moisture on Au/SiO_2, in our Au–Ag alloy system, Ag would play an important role for the adsorption and activation of oxygen at lower temperatures. With the rise in reaction temperature, the desorption of oxygen would dominate, so that the reaction activity decreased. Above a temperature of 160 °C, the temperature behavior of the catalytic activity of the alloy nanoparticles returns to normal and is similar to that of pure gold nanoparticles.

The third feature of the Au–Ag alloy catalysts was their complete deactivation at room temperature in the presence of an excess amount of H_2. It has been suggested that supported gold catalysts can selectively oxidize CO to CO_2 in the presence of rich H_2 at low temperatures [55–59]. Even Ag/SiO_2 has been reported to selectively catalyze CO oxidation at low temperatures [50]. Generally, the introduction of H_2 into the reaction stream will decrease CO conversion slightly. How-

ever, in our case, the presence of 60% H_2 in the feed gas greatly improved the catalytic activity of Au@MCM, which is similar to the effect of moisture on Au/SiO_2 [54]. This may be due to the generation of water vapor from the oxidation of hydrogen. And water, in turn, promotes CO oxidation. In contrast, the Au–Ag (3:1) alloy catalyst lost its activity completely when rich H_2 was introduced into the reaction stream. As suggested above, the adsorption of oxygen to the Au–Ag alloy at low temperatures plays a key role. However, the adsorption of oxygen to the Au–Ag alloy is not very strong [41]; excess H_2 may completely cover the surface and block the adsorption sites for oxygen. In the alloy catalytic activity test, when a large amount of H_2 was present in the reaction stream, no consumption of O_2 was observed, implying that neither CO nor H_2 was oxidized upon the addition of H_2 to the reaction stream. This confirms that H_2 competes with O_2 rather than with CO.

4.3. A possible mechanism for the Au–Ag alloy system

Kondarides and Verykios studied the adsorption of oxygen on supported Au–Ag alloy catalysts by microgravimetric and TPD techniques [41]. They found that the presence of Au on the Ag surfaces leads to the destruction of multiple sites necessary for dissociative oxygen adsorption, indicated by the activation energy for atomic oxygen adsorption, which increased from 4 to 40 kJ/mol when the surface Au content increased from zero to 24 at%. On the other hand, the activation energy for molecular oxygen adsorption decreased from 44 to 17 kJ/mol, indicating that molecular oxygen adsorption to Ag is favored by the presence of Au. Our EPR results confirmed the existence of O_2^- species on the catalyst surface, and its intensity varied with the Au/Ag ratio. This is in agreement with the observation of Kondarides et al. that the molecular oxygen adsorption to the Ag surface can be modified by the addition of Au. In addition, our XPS results also confirmed that Au–Ag alloy catalysts have a greater tendency to lose electrons than do the corresponding monometallic catalysts. Since oxygen adsorption and activation are the key steps in CO oxidation, the exceptionally high activity at low temperature of Au–Ag alloy catalysts implies that oxygen can be adsorbed and activated on the alloy catalyst surface at low temperatures. Therefore, we believe that the adsorption and activation of oxygen must take place on Ag, and the presence of Au helps the molecular adsorption of oxygen and formation of the O_2^- species on the Ag surface. Meanwhile, the adsorption of CO occurs on Au. For the reaction between O_2^- and adsorbed CO to occur, the Au and Ag must be in proximity to each other so that the two adsorbed species can interact. Based on our experimental observation and the above reasoning, a mechanism was proposed as shown in Scheme 1. The alloy can adsorb CO and O_2 on neighboring sites. Electron transfer from Ag to the antibonding orbital of oxygen molecule helps weaken its chemical bond. With a neighboring adsorbed CO, the oxygen transfer reaction could then occur easily. From the proposed scheme, one may expect the surface composition for optimum catalysis to be close to an Au/Ag ratio of 1. Indeed, we find the surface composition for the catalyst of best activity has an Au/Ag ratio of 0.75, whereas its nominal Au/Ag ratio is 3:1 (see Table 2).

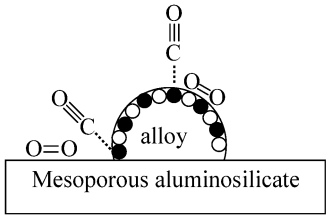

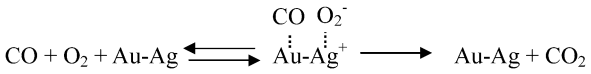

Scheme 1.

5. Conclusion

In this work, Au–Ag alloy nanoparticles on a mesoporous support were prepared by a novel one-pot method. The mesoporous support helps the dispersion of the nanoparticles of Au–Ag alloy, and the mesopores facilitate the transport of molecules. Although thus formed alloy nanoparticles are relatively large, they exhibited exceptionally high activity for CO oxidation at low temperatures. Compared with monometallic Au or Ag catalysts, the alloy catalysts showed an unusual activity profile with the reaction temperature, and excess hydrogen in the feed gas deactivated the catalysis completely. In this alloy system, Ag plays a key role in oxygen activation, and Au sites adsorb CO while assisting the activation of oxygen by decreasing the activation energy for molecular adsorption of oxygen, showing a strongly synergistic effect between Au and Ag. The best-performing Au–Ag alloy catalyst is the one with a nominal Au/Ag ratio of 3:1. Low-temperature oxidation of CO catalyzed by Au–Ag alloy nanoparticles is of fundamental interest and has application potential.

In summary, we have created a bifunctional catalytic system with the use of nanoparticles of alloys. We believe our approach could be generalized to many other catalytic reactions. Following this general approach to search for other alloy nanocatalyst systems for various reactions would be rewarding.

Acknowledgments

This work was supported by a grant from the Ministry of Education of Taiwan through the Academy Excellence Program. T.-S.L. acknowledges partial support from the NSF and PRF. We also acknowledge technical assistance from Prof. H.P. Lin, Mr. C.C. Huang, and M.L. Lin.

References

[1] M. Haruta, T. Kobayashi, H. Sano, N. Yamada, Chem. Lett. (1987) 405.
[2] M. Haruta, Chem. Record 3 (2003) 75.
[3] M. Haruta, Catal. Today 36 (1997) 153.
[4] G.C. Bond, D. Thompson, Catal. Rev. Sci. Eng. 41 (1999) 319.
[5] H.H. Kung, M.C. Kung, C.K. Costello, J. Catal. 216 (2003) 425.
[6] F. Boccuzzi, A. Chiorino, M. Manzoli, P. Lu, T. Akita, S. Ichikawa, M. Haruta, J. Catal. 202 (2001) 256.
[7] M. Valden, X. Lai, D.W. Goodman, Science 281 (1998) 1647.
[8] D.C. Meier, D.W. Goodman, J. Am. Chem. Soc. 126 (2004) 1892.
[9] N. Lopez, T.V.W. Janssens, B.S. Clausen, Y. Xu, M. Mavrikakis, T. Bligaard, J.K. Norskov, J. Catal. 223 (2004) 232.
[10] W.T. Wallace, R.L. Whetten, J. Phys. Chem. B 104 (2000) 10964.
[11] F. Moreau, G.C. Bond, A.O. Taylor, Chem. Commun. (2004) 1642.
[12] H. Liu, A.I. Kozlov, A.P. Kozlova, T. Shido, K. Asakura, Y. Iwasawa, J. Catal. 185 (1999) 252.
[13] Y.J. Chen, C.T. Yeh, J. Catal. 200 (2001) 59.
[14] A.I. Kozlov, A.P. Kozlova, K. Asakura, Y. Matsui, T. Kogure, T. Shido, Y. Iwasawa, J. Catal. 196 (2000) 56.
[15] A.P. Kozlova, S. Sugiyama, A.I. Kozlov, K. Asakura, Y. Iwasawa, J. Catal. 176 (1998) 426.
[16] M.M. Schubert, S. Hackenberg, A.C. van Veen, M. Muhler, V. Plzak, R.J. Behm, J. Catal. 197 (2001) 113.
[17] S. Arrii, F. Morfin, A.J. Renouprez, J.L. Rousset, J. Am. Chem. Soc. 126 (2004) 1199.
[18] W.S. Epling, G.B. Hoflund, J.F. Weaver, J. Phys. Chem. 100 (1996) 9929.
[19] J.D. Grunwaldt, M. Maciejewski, O.S. Becker, P. Fabrizioli, A. Baiker, J. Catal. 186 (1999) 458.
[20] C.K. Costello, J. Guzman, J.H. Yang, Y.M. Wang, M.C. Kung, B.C. Gates, H.H. Kung, J. Phys. Chem. B 108 (2004) 12529.
[21] S. Carrettin, P. Concepcion, A. Corma, J.M. Lopez Nieto, V.F. Puntes, Angew. Chem. Int. Ed. 43 (2004) 2538.
[22] H. Häkkinen, S. Abbet, A. Sanchez, U. Heiz, U. Landman, Angew. Chem. Int. Ed. 42 (2004) 1297.
[23] Y. Xu, M. Mavrikakis, J. Phys. Chem. B 107 (2003) 9298.
[24] G. Mills, M.S. Gordon, H. Metiu, J. Chem. Phys. 118 (2003) 4198.
[25] T.S. Kim, J.D. Stiehl, C.T. Reeves, R.J. Meyer, C.B. Mullins, J. Am. Chem. Soc. 125 (2003) 2018.
[26] J.D. Stiehl, T.S. Kim, S.M. McClure, C.B. Mullins, J. Am. Chem. Soc. 126 (2004) 1606.
[27] M. Okumura, S. Tsubota, M. Iwamoto, M. Haruta, Chem. Lett. (1998) 315.
[28] M. Okumura, S. Tsubota, M. Haruta, J. Mol. Catal. A 199 (2003) 73.
[29] A.M. Venezia, L.F. Liotta, G. Pantaleo, V. La Parola, G. Deganello, A. Beck, Zs. Koppany, K. Frey, D. Horvath, L. Guczi, Appl. Catal. A 251 (2003) 359.
[30] L. Guczi, A. Beck, A. Horvath, Zs. Koppany, G. Stefler, K. Frey, I. Sajo, O. Geszti, D. Bazin, J. Lynch, J. Mol. Catal. A 204–205 (2003) 545.
[31] A. Baiker, M. Maciejewski, S. Tagliaferri, P. Hug, J. Catal. 151 (1995) 407.
[32] H. Nakatsuji, H. Nakai, Chem. Phys. Lett. 174 (1990) 283.
[33] H. Nakatsuji, H. Nakai, Can. J. Chem. 70 (1992) 404.
[34] H. Nakatsuji, Z.M. Hu, H. Nakai, K. Ikeda, Surf. Sci. 387 (1997) 328.
[35] A. Sandell, P. Bennich, A. Nilsson, B. Hernnäs, O. Björneholm, N. Mårtensson, Surf. Sci. 310 (1994) 16.
[36] H.P. Lin, Y.S. Chi, J.N. Lin, C.Y. Mou, B.Z. Wan, Chem. Lett. (2001) 1116.
[37] J.H. Liu, A.Q. Wang, H.P. Lin, C.Y. Mou, J. Phys. Chem. B 109 (2005) 40.
[38] J.F. Moulder, W.F. Stickle, P.E. Sobol, K.D. Bomben, in: J. Chastain (Ed.), Handbook of X-Ray Photoelectron Spectroscocy, Perkin–Elmer, Eden Prairie, MN, 1992.
[39] M.C. Chao, H.P. Lin, C.Y. Mou, Chem. Lett. 33 (2004) 672.
[40] H.P. Lin, C.P. Tsai, Chem. Lett. 32 (2003) 1092.
[41] D.I. Kondarides, X.E. Verykios, J. Catal. 158 (1996) 363.
[42] M.P. Mallin, C.J. Murphy, Nano Lett. 2 (2002) 1235.
[43] I. Lee, S.W. Han, K. Kim, Chem. Commun. (2001) 1782.
[44] S. Link, Z.L. Wang, M.A. EI-Sayed, J. Phys. Chem. B 103 (1999) 3529.
[45] H.Z. Shi, L.D. Zhang, W.P. Cai, J. Appl. Phys. 87 (2000) 1572.
[46] J. Radnik, C. Mohr, P. Claus, Phys. Chem. Chem. Phys. 5 (2003) 172.
[47] A. Zwijnenburg, A. Goossens, W.G. Sloof, M.W.J. Crajé, A.M. van der Kraan, L. Jos de Jongh, M. Makkee, J.A. Moulijn, J. Phys. Chem. B 106 (2002) 9853.
[48] T. Shibata, B.A. Bunker, Z.Y. Zhang, D. Meisel, C.F. Vardeman, J.D. Gezelter, J. Am. Chem. Soc. 124 (2002) 11989.
[49] M. Okumura, J.M. Coronado, J. Soria, M. Haruta, J.C. Conesa, J. Catal. 203 (2001) 168.
[50] Z.P. Qu, M.J. Cheng, X.L. Dong, X.H. Bao, Catal. Today 93–95 (2004) 247.
[51] A.M. Venezia, L.F. Liotta, G. Deganello, Z. Schay, D. Horváth, L. Guczi, Appl. Catal. A 211 (2001) 167.
[52] A. McNeillie, D.H. Brown, W. Ewen Smith, J. Chem. Soc., Dalton Trans. 767 (1980).
[53] Y. Iizuka, A. Kawamoto, K. Akita, M. Daté, S. Tsubota, M. Okumura, M. Haruta, Catal. Lett. 97 (2004) 203.
[54] M. Daté, M. Okumura, S. Tsubota, M. Haruta, Angew. Chem. Int. Ed. 43 (2004) 2129.
[55] R.J.H. Grisel, B.E. Nieuwenhuys, J. Catal. 199 (2001) 48.
[56] R.M. Torres Sanchez, A. Ueda, K. Tanaka, M. Haruta, J. Catal. 168 (1997) 125.
[57] M.J. Kahlich, H.A. Gasteiger, R.J. Behm, J. Catal. 182 (1999) 430.
[58] G.K. Bethke, H.H. Kung, Appl. Catal. A 194 (2000) 43.
[59] B. Schumacher, Y. Denkwitz, V. Plzak, M. Kinne, R.J. Behm, J. Catal. 224 (2004) 449.